Constraints on the interpretation of *S*-to-*P* receiver functions

David C. Wilson,[1] D. A. Angus,[2] James F. Ni[2] and Stephen P. Grand[1]

[1]*University of Texas, Austin, Department of Geological Sciences, Austin, TX, USA. E-mail: davew@geo.utexas.edu* [2]*New Mexico State University, Department of Physics, Las Cruces, NM, USA*

Accepted 2006 February 28. Received 2006 February 27; in original form 2005 August 17

SUMMARY

We present results from forward modelling to study the feasibility of using *S*-to-*P* converted phases to image the seismic discontinuity structure of the crust and upper mantle. We show that a significant level of *P*-wave energy arriving before the direct *S*-wave arrival can interfere with the *S*-to-*P* converted phases of interest and may result in *Sp* receiver function phases that do not represent true earth structure. The source of this *P*-wave energy is attributable to a number of phases, including those that have undergone multiple reflections off the Earth's surface. For deep focus earthquakes (300–600 km deep), a significant amount of *P*-wave energy is observed from *pPPP*, *pPPPP* and *sPPPP* phases, and arrives within the same time window as predicted for *S*-to-*P* converted phases from the direct *S* phase arrival. Furthermore, for earthquakes at all depths, interfering *P*-wave energy arrives within the same time window as predicted for *S*-to-*P* converted phases from the *SKS* phase arrival, limiting the usefulness of *SKSp* receiver functions for upper mantle imaging. To isolate true *Sp* receiver function phases from contamination due to other *P*-wave phases, we find it necessary to stack receiver functions from a range of epicentral distances and depths in order to aid the suppression of noise and other unwanted phases. We provide constraints on the noise levels to be expected as a function of epicentral distance and earthquake depth. We find that the lowest noise levels are achievable by restricting epicentral distance to less than 75 degrees and the depth of earthquakes used to less than 300 km.

Key words: converted phases, receiver functions, teleseismic phases.

1 INTRODUCTION

The *Ps* receiver function method, which utilizes *P*-to-*S* converted seismic phases beneath a recording station, has been an invaluable tool in imaging the seismic discontinuity structure of the crust and upper mantle (e.g. Sheehan *et al*. 1995; Yuan *et al*. 1997; Li *et al*. 2002; Wilson *et al*. 2005). The basic premise behind the *Ps* receiver function method is that the incoming direct *P*-wave energy arrives before any direct *S*-wave energy from a given earthquake, so that any *S* wave phases recorded contemporaneously with the incoming *P* wavefield must be *P*-to-*S* converted energy. *Ps* receiver function analysis emphasizes *P*-to-*S* converted arrivals due to sub- surface velocity and impedance discontinuities via signal deconvolution between horizontal and vertical component seismograms (e.g. Langston 1977; Vinnik 1977; Langston 1979; Owens *et al*. 1984; Ammon 1991). This cross-component deconvolution removes the common factors of instrument response and source function from the seismogram resulting in a receiver function that is predominantly controlled by the velocity and impedance discontinuity structure of the crust and upper mantle along the ray path. One major limitation in upper mantle imaging with *Ps* receiver functions arises from the fact that sharp velocity contrasts at the Moho and deep sedimentary basins introduce large amplitude multiples that produce imaging artifacts that can potentially overprint deeper structure. For instance, Moho multiples contain significant energy that can

obscure arrivals from possible subcrustal discontinuities such as the lithospheric–asthenospheric boundary (Farra & Vinnik 2000; Wilson & Aster 2005).

In contrast to *Ps* receiver functions, the *Sp* receiver function method attempts to isolate *S*-to-*P* mode converted energy associated with direct *S* arrivals (Farra & Vinnik 2000). One potential advantage of *Sp* receiver functions is that converted *P*-wave energy travels faster than the incoming *S* wavefield. Thus, *Sp* receiver functions are relatively free of contaminating energy arising from first-order multiples, allowing upper mantle imaging with fewer artifacts. Recent applications of *Sp* receiver function methodology have taken advantage of this aspect to produce images of the Moho, lithosphere/asthenosphere boundary and other possible upper mantle low-velocity zones (e.g. Farra & Vinnik 2000; Vinnik *et al*. 2003, 2004, 2005; Li *et al*. 2004; Wittlinger *et al*. 2004; Kumar *et al*. 2005).

S-to-*P* converted phases observed on raw seismograms have been used to investigate crust and upper mantle structure (e.g. Jordan & Frazer 1975; Langston 1977; Baag & Langston 1986; Bock 1988; Owens & Zandt 1997). In a global study of *S*-to-*P* converted waves, Bock & Kind (1991) find that, within the time window suitable for observation of *S*-to-*P* converted phases (immediately preceding the *S*-wave arrival), both real and synthetic data exhibit considerable amplitude variation and significant ambient energy levels. They postulate that this may be due to interference from precursors to *sS*, *ScS* and *SKS* phases. Within this same time window, Vinnik & Romanowicz (1991) identify the presence of certain phases (specifically *sPPP* and *sPPPP*) that have been reflected off the Earth's surface multiple times. They also identify *P*-wave energy that may be due to *S*-to-*P* scattering from lateral heterogeneities in the lithosphere between the source and receiver, having a similar ray path to the teleseismic phase *SP*. In a synthetic seismogram study, Bock (1994) also identified the presence of phases that have undergone multiple reflections off the Earth's surface and arrive as precursors to *S*, *SKS* and *ScS*. Bock notes that these precursors can have similar amplitude to and arrive in the same time window as upper mantle *S*-to-*P* converted phases. The presence of the various *P*-wave phases mentioned above violates a basic premise of the *Sp* receiver function method; the assumption that all *P*-wave energy immediately preceding the *S*-wave arrival was produced by mode conversion from the *S*-wave arrival. Receiver function deconvolution may enhance the amplitude of this interfering *P*-wave energy and result in a receiver function that may contain significant energy that does not represent true *Sp* receiver function phases.

To reduce noise in receiver function processing, a move-out time correction is generally applied such that many receiver functions can be stacked (Langston 1977; Vinnik 1977; Farra & Vinnik 2000) so that random noise within individual receiver functions will cancel. This assumes that the noise is random or that the unwanted energy has moveout characteristics that are significantly different from the true receiver function phases. If the interfering *P*-wave phases arriving just before the *S* wavefield (Bock & Kind 1991; Vinnik & Romanowicz 1991; Bock 1994) have large enough amplitude or if the moveout characteristics of these phases are similar to *Sp* receiver function phases, they may cause considerable artifacts in *Sp* receiver function stacks and in the resulting *Sp* receiver function images. In this study we create a suite of synthetic data sets to determine the origin and magnitude of interfering *P*-wave phases immediately preceding the *S*-wave arrival. We assess the feasibility of using *Sp* receiver functions to image the crust and upper mantle and provide constraints on the usable earthquake epicentral distance and depth ranges in order to minimize imaging artefacts.

2 SYNTHETIC DATA

We create a series of synthetic seismogram (displacement) data sets using the reflectivity method

(Fuchs & Mueller 1971) for the full *P- Sv* system using the 1-D PREM reference earth model (Dziewonski & Anderson 1981) with a crustal thickness of 70 km (Fig. 1). We have selected this velocity model because of its large velocity dis- continuities at 220 and 400 km depth. The resulting receiver function images, if properly imaged, will show distinct phases at 70, 220 and 400 km depths with minimal energy at other depths. Seismograms are calculated for earthquakes at 30, 300 and 600 km depth and epicentral distances from 60 to 120 degrees using periods from 4 to 120s (Figs 1–3). We use a double–couple source with 25 degrees dip (thrust fault), oriented to optimize *Sv* radiation for direct *S* and *SKS* take-off angles. Individual phases in Figs 1–3 have been identified using the TauP traveltime toolkit (Crotwell *et al*. 1999).

Horizontal (radial) and vertical synthetic seismograms for a shallow (30 km source depth) earthquake are shown in Fig. 2. The direct *S* (red) and *SKS* (green) arrivals are clearly visible, with approximately equal amplitudes on the horizontal component (with opposite polarity). The *SKS* arrival has lower amplitude on the vertical component with respect to the direct *S* arrival because the angle of incidence of the *SKS* phase (6–12 degrees) is closer to vertical than the *S* phase incidence angle (19–25 degrees). Following closely behind the *S* arrival is the *SP* phase (magenta). While this phase al- ways arrives after the *S* arrival, it can generate precursors that may arrive earlier. One such precursor, caused by an underside reflection off the Moho, can be seen approximately 15 s before the *SP* arrival (Fig. 2, dashed magenta), especially at distances of 90–120 degrees. Scattering from lateral heterogeneities in the lithosphere between the source and receiver (not included in our synthetic seismograms) can also produce significant precursors to the *SP* phase arrival (Vinnik & Romanowicz 1991).

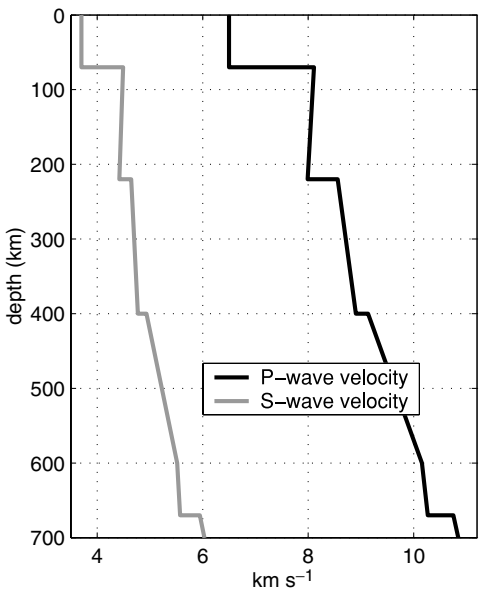

Figure 1. Velocity model used for generating synthetic data.

The predicted time window for *S*-to-*P* converted phases from upper mantle discontinuities (less than 400 km depth) are shown for both the direct *S* (red dashed) and *SKS* (green dashed) phase arrivals (Fig. 2). At epicentral distances between 75–95 degrees, these windows have significant overlap and may make it difficult to discern the origin of converted phases observed within this time window. A significant amount of energy is observed, primarily on the vertical component, immediately preceding the *SKS* arrival, particularly at distances greater than 90 degrees. We

quantify the magnitude of this energy by computing the square root of the mean squared (rms) vertical component amplitude in a 60 s window preceding the first arriving *S* phase relative to the horizontal component rms value in a 10s window encompassing the first arriving *S* phase. For the shallow earthquake (Fig. 2) median vertical component noise levels for distances greater than 90 degrees are 8.9 per cent compared to 2.7 per cent for distances less than 90 degrees. Based on predicted traveltimes, we have identified this energy as multiply reflected phases from the Earth's surface. For the shallow earthquake, this energy is primarily due to *pPPPP* and *pPPPPP* phases. Since these phases have undergone multiple reflections off the Earth's surface and have traversed crust and upper mantle discontinuities multiple times, they consist of a series of precursory and post-cursory ar- rivals that are spread out over a significant time window (up to 60s), and do not appear as a single distinct arrival (e.g. Gutenberg 1960). These phases overlap the *SKS* arrival as well as the time window that may contain *SKSp* converted phases. Note that although we are referring to the magnitude of this energy arriving prior to the *S* wave as a noise level, this time window also contains *S*-to-*P* converted phases which contribute to the rms amplitude. However, *S*-to-*P* converted phase amplitudes should only change gradually as a function of epicentral distance and earthquake depth (due to gradual changes in source radiation patterns and incidence angles) and the majority of the changes in noise levels we observe are due to phases have undergone multiple reflections off the Earth's surface.

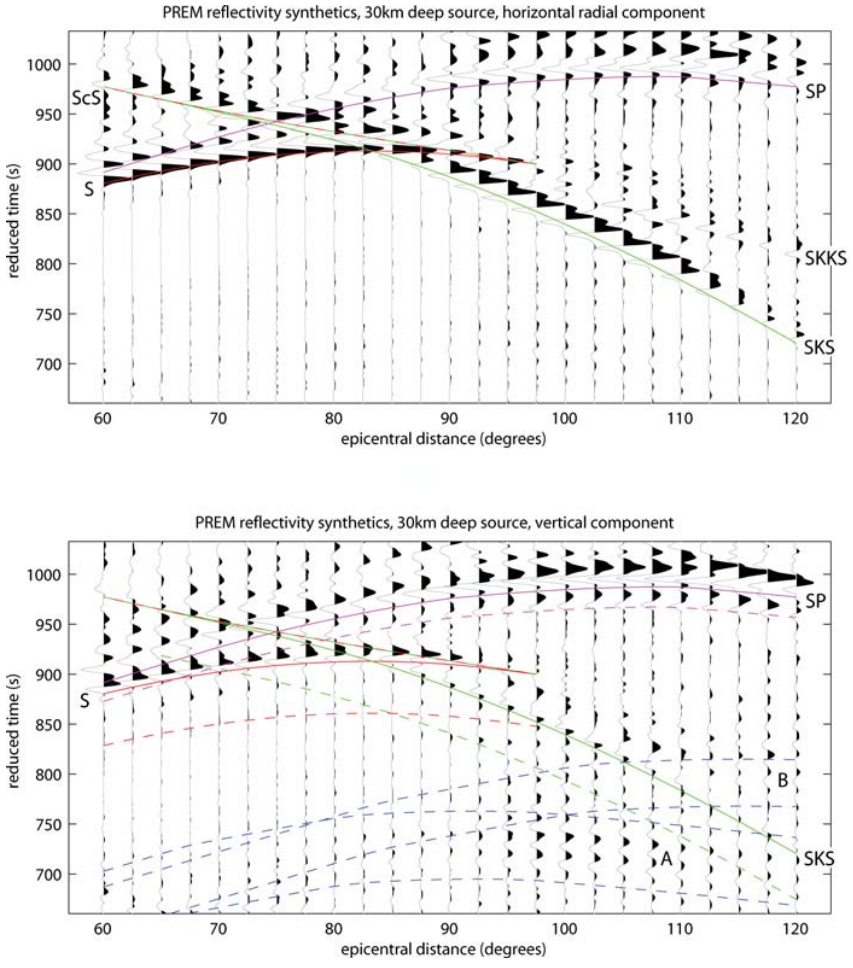

Figure 2. Synthetic data for a 30-km-deep earthquake. Solid lines indicate the arrival times of

direct *S* (Red), *SKS* (green) and *SP* (magenta) phases. Dashed blue lines indicate the time windows (as a function of epicentral distance) for arrivals from: (a) *pPPPP* and (b) *pPPPPP*. The timescales used in Figs 1–3 have been reduced using a reduction velocity of $V = 11$ km s^{-1} and a reference time of $t\,0 = -392$s. Thus the timescale represents the actual phase arrival time less the quantity $(t\,0 + X/V)$, where X is the earthquake epicentral distance in km. The dashed red and green lines in Figs 2–4 indicate the predicted time window for *S*-to-*P* converted phases from upper mantle discontinuities (less than 400 km depth) for the direct *S* and *SKS* phase arrivals, respectively. The dashed magenta lines indicates a *SP* precursor caused by an underside reflection off the Moho.

Horizontal (radial) and vertical synthetic data for an intermediate depth (300 km) earthquake are shown in Fig. 3. Arrivals from *S*, *SKS* and *SP* phases are still clearly observed as well as the Moho *SP* precursor phase predominantly seen on the vertical component. As the earthquake source moves deeper, phases that have been reflected multiple times off the Earth's surface arrive slightly later, creating even greater overlap with the *SKS* arrival as well as the time window that may contain *SKSp* converted phases. In comparison with Fig. 2, there is an overall increase in the ambient signal level, primarily on the vertical component, for the time window preceding the *S* arrival. Computed median vertical component noise levels for distances less than 90 degrees are 5.2 per cent compared to 2.7 per cent for the same distance range for the shallow earthquake. Horizontal (radial) and vertical synthetic data for a deep (600 km source depth) earthquake are shown in Fig. 4. Shown are four time windows containing energy from phases that have experienced multiple reflections off the Earth's surface. These phases now overlap both the direct *S* and *SKS* arrivals. In comparison to both Figs 2 and 3, there is an overall increase in the ambient signal level for the time window preceding the *S* arrival. Computed median vertical component noise levels for distances less than 90 degrees have now increased to 10.9 per cent for this deep earthquake.

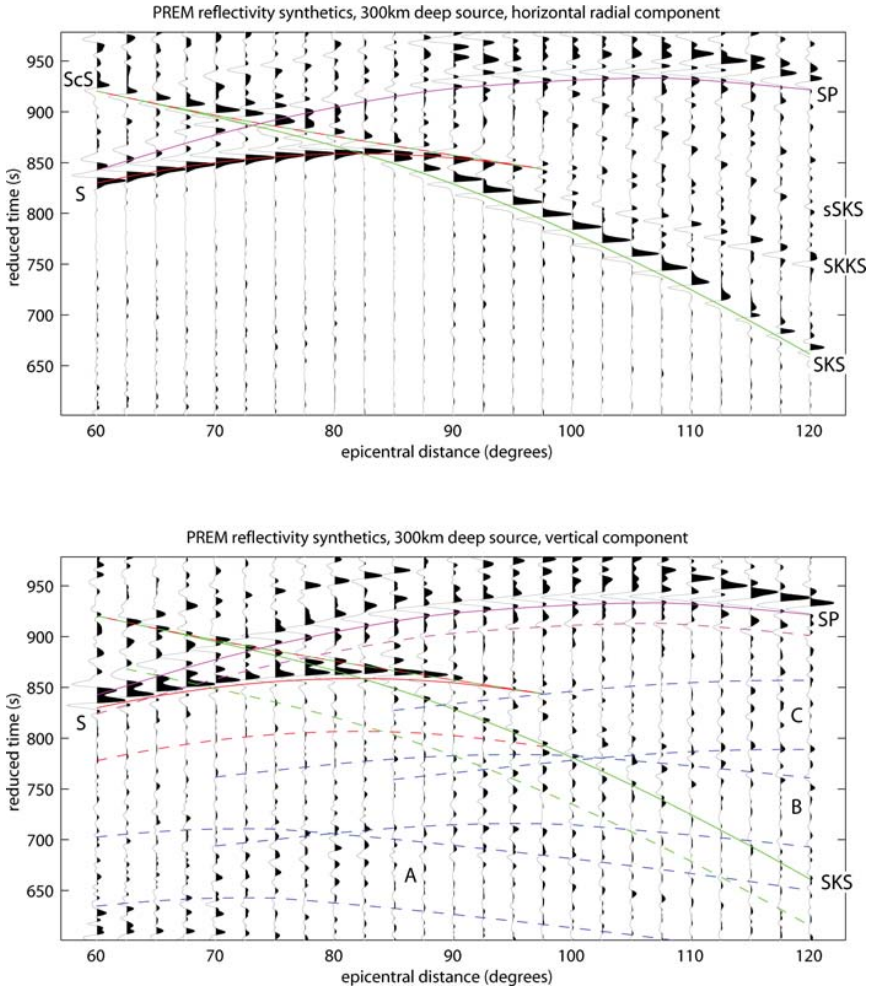

Figure 3. Synthetic data for a 300-km-deep earthquake. Dashed blue lines indicate time windows for arrivals from: (a) *pPPP*, (b) *pPPPP* and (c) *pPPPPP*. Note the generally larger amplitude vertical component ambient signal level arriving prior to the *S* and *SKS* phase arrivals as compared to Fig. 2.

3 SP RECEIVER FUNCTIONS

In typical *Ps* receiver function processing, seismograms are rotated from the vertical, north and east (Z, N, E) components into vertical, radial and transverse (Z, R, T) components (e.g. Langston 1977; Owens *et al*. 1984; Ammon 1991). To produce a radial *Ps* receiver function, the vertical (Z) component is then deconvolved from the radial (R) component. This assumes that the Z component is a good representation of the incoming *P* wavefield and that the R component contains predominantly *P*-to-*S* converted waves. This assumption is adequate for *Ps* receiver function processing because the incidence angle of *P*-to-*S* converted waves from the usable epicentral distance range (35–85 degrees) is only 10–15 degrees from vertical. For *Sp* receiver functions, however, the incidence angle of *S*-to-*P* converted waves can be as great as 45 degrees from vertical requiring rotation into local ray coordinates (i.e. the incidence angle of the incoming seismic energy) in order to isolate the primary and converted phases. This rotation is accomplished by either calculating a theoretical ray angle based on a reference velocity model (e.g. Farra & Vinnik 2000), or by estimation of an empirical ray angle by linearizing particle

motion of the first few cycles of the *P* wave (e.g. Vinnik 1977). Estimating an empirical incidence angle may help mitigate errors in rotation caused by unknown near surface velocity structure, or regions with significant lateral velocity variation. However, in the presence of low signal to noise ratios, this method may result in a poor estimate of the true incidence angle.

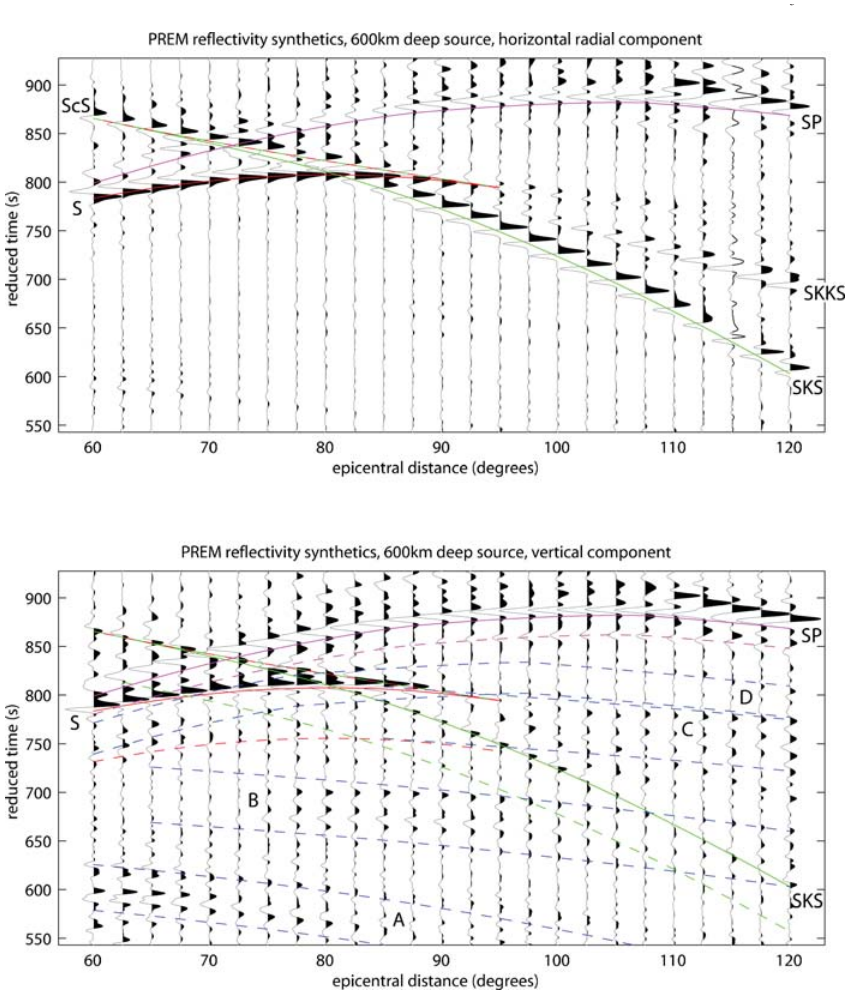

Figure 4. Synthetic data for a 600-km-deep earthquake. Dashed blue lines indicate time windows for arrivals from: (a) *pPP*, (b) *pPPP*, (c) *pPPPP* and (d) *sPPPP*. The vertical component ambient signal level prior to the *S* and *SKS* phase arrivals is now much larger in amplitude than observed in both Figs 2 and 3.

Figs 5–7 show receiver functions calculated from the direct *S* or *SKS* arrivals (depending on which phase arrives earlier for a given epicentral distance) shown in Figs 2–4. Components have been rotated into the longitudinal *P*- and *S*v-wave directions determined from theoretical incidence angles. The *S*v component is tapered around a 15 s. window encompassing the direct *S* or *SKS* arrival, and is then deconvolved from the *P* component using water-level deconvolution. A range of water levels are examined, and the level that gives the optimal trade-off between fitting the data and producing a receiver function with a minimal amount of ringing is selected (determined by minimizing the second-order derivative of the receiver function). Receiver functions have been converted to depth to allow comparison using a common depth axis. For relatively short epicentral distances (less than 70 degrees), arriving *S* wavefields encounter

discontinuities at depth (e.g. 400 and 220 km) at sub-horizontal incidence angles and do not produce pre-critical *P*-wave transmissions. The resulting receiver functions from these short epicentral distances show diminished receiver function amplitude at large depths after depth conversion.

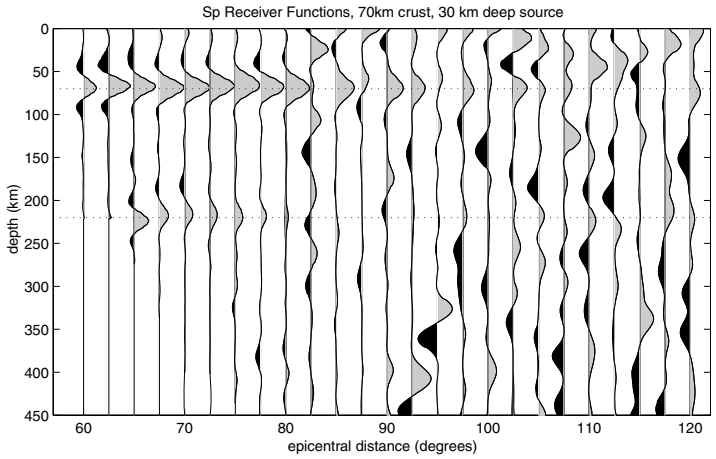

Figure 5. *Sp* receiver functions calculated from the synthetic data set in Fig. 2.

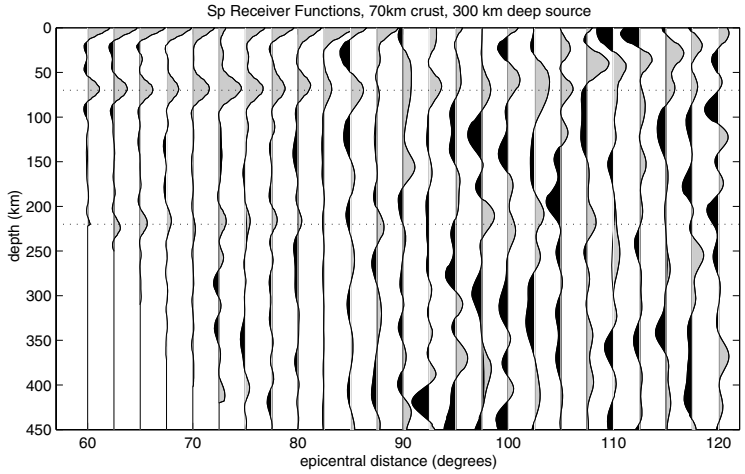

Figure 6. *Sp* receiver functions calculated from the synthetic data set in Fig. 3.

For epicentral distances less than 80 degrees, *Sp* receiver functions calculated for the shallow (30 km) earthquake (Fig. 5) show a clear Moho discontinuity at 70 km and an upper mantle discontinuity at 220 km as expected from the PREM model. At a distance of 82.5 degrees, close to where the direct *S* and *SKS* arrivals begin to interfere with one another (Fig. 2), the calculated receiver function fails to properly image the Moho and 220 km discontinuity. This is because the time window used for the source estimate on the *S*v component contains both the direct *S* and the *SKS* arrival (having opposite polarity), and so provides a poor source estimate for deconvolution. At distances greater than 85 degrees, where the *SKS* phase arrives first, the Moho is present at the correct depth on approximately two-thirds of the receiver functions, but the 220 km discontinuity only appears at the correct depth on less than 1/3 of calculated receiver functions. At distances greater than 90 degrees, there is a high level of erroneous *Sp* receiver function phases that

correspond to the time window of observed interfering *P*-wave energy (Fig. 2) caused by phases that have undergone multiple reflections from the Earth's surface. We quantify the receiver function noise level by computing the rms receiver function value from 100–200 km depth (where there should be zero amplitude) relative to the rms receiver function value of a window encompassing the Moho signal (65–75 km depth). We measure noise levels relative to the Moho because it is the strongest seismic discontinuity in our velocity model (Fig. 1) with contrasts of –20, –18 and –14 per cent in *Vp*, *Vs* and density, respectively. Computed noise levels are given in Table 1 and indicate median noise levels of 7.2, 20.4 and 71.7 per cent for the distance ranges 60–75, 75–95 and 85–120 degrees, respectively, for this earthquake.

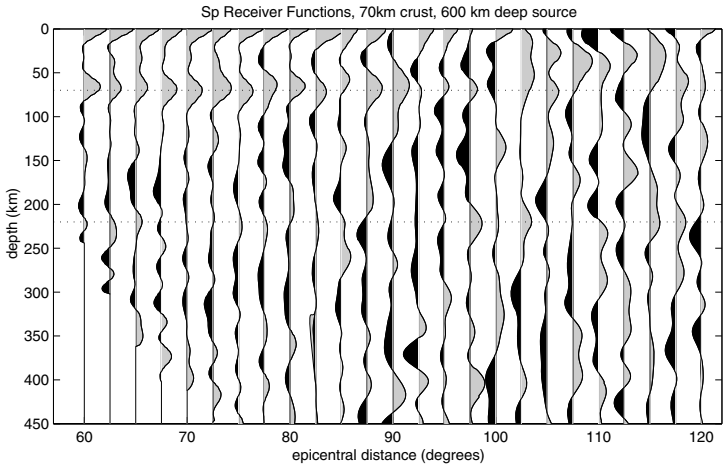

Figure 7. *Sp* receiver functions calculated from the synthetic data set in Fig. 4.

Receiver functions calculated for an intermediate depth (300 km) earthquake are shown in Fig. 6. At distances less than 80 degrees, the Moho and 220 km discontinuities are clearly observed and receiver function noise levels are only slightly higher (8.4 vs. 7.2 per cent) than for the shallow earthquake (Fig. 5). At distances greater than 85 degrees, the Moho is imaged to the correct depth on approximately 60 per cent of calculated receiver functions, whereas the 220 km discontinuity is imaged to the correct depth on only 20 per cent of the receiver functions. At distances greater than 85 degrees, we observe an even higher level (75.0 vs. 71.7 per cent) of erroneous receiver function phases than observed for the shallow earthquake source (Fig. 5; Table 1), and this again corresponds to the time window of the observed interfering *P*-wave energy (Fig. 3).

For a deep (600 km) earthquake (Fig. 7) we observe that the Moho is clearly imaged on *Sp* receiver functions for epicentral distances less than 80 degrees, whereas the 220 km discontinuity only appears at the correct depth on approximately two-thirds of calculated receiver functions within this distance range. For epicentral distances greater than 85 degrees, the Moho is imaged at the correct depth on 40 per cent of calculated receiver functions, and the 220 km discontinuity only appears at the correct depth on 27 per cent. Receiver functions at all epicentral distances exhibit a high level of erroneous *Sp* receiver function phases (18.6, 37.0 and 100.9 per cent for the distance ranges 60–75, 75–95 and 85–120 degrees, respectively; Table 1) because the time window of observed interfering *P*-wave energy for a deep earthquake (Fig. 4) overlaps both the direct *S* and *SKS* phases.

Table 1. Receiver function noise levels calculated by computing the rms receiver function value from 100–200 km depth relative to the rms receiver function value of a window encompassing

the Moho signal (65– 75 km depth).

Distance range	60–75	75–95	85–120	60–120
Median, 30 km depth	0.0722	0.2042	0.7167	0.2094
Median, 300 km depth	0.0841	0.2533	0.7503	0.3312
Median, 600 km depth	0.1861	0.3700	1.0093	0.4114
30 km depth, stacked	0.0391	0.0729	0.1334	0.0676
300 km depth, stacked	0.0284	0.1432	0.2677	0.1293
600 km depth, stacked	0.1591	0.2117	0.2391	0.1558
Less than 300 km, stacked	0.0292	0.0627	0.1214	0.0684
All depths, stacked	0.0463	0.0594	0.1151	0.0739
Less than 300 km, bootstrap	0.0244	0.0411	0.0750	0.0425
All depths, bootstrap	0.0371	0.0495	0.0849	0.0565

4 DISCUSSION

To study the possibility that stacking *Sp* receiver functions for a range of epicentral distances might enhance true *Sp* receiver function phases and de-emphasize (or cancel) any erroneous phases, we have created a series of stacked traces from the calculated receiver functions in Figs 5–7. The resulting receiver function stacks are shown in Fig. 8. Stacked traces from earthquakes at all three depths exhibit a clear Moho signal for all stacking distance ranges. For the shallow and intermediate depth earthquakes, stacked receiver functions from 60–75 degrees epicentral distance exhibit minimal erroneous receiver function phases (3.9 and 2.8 per cent, respectively; Table 1) and clearly show converted phases from discontinuities at 70, 220 and 400 km depth. The 400 km discontinuity is lower in amplitude for the shallow earthquake since many of *Sp* ray paths that went into this stack have turned critical prior to reaching 400 km depth (Fig. 5). For this same distance range (60–75 degrees), stacked receiver functions from the deep earthquake show a significant level of erroneous receiver function phases (15.9 per cent). Increasing the stacking distance range to include distances where *S* and *SKS* phases are arriving simultaneously (75–95 degrees), or distances where the *SKS* phase arrives first (85–120 degrees), results in an increase in the level of erroneous receiver function phases ob- served on stacked traces from earthquakes at all depths (Table 1). Phases in the stacked receiver functions (Fig. 8) indicate that the erroneous receiver function phases observed at distances greater than 75 degrees for the shallow and intermediate depth earthquakes, and at all distances for the deep earthquake, do not have a distribution that is sufficiently random to be cancelled or significantly de-emphasized by simple stacking of several receiver functions from a range of epicentral distances for a single earthquake depth. This may be because the erroneous receiver function phases do not have sufficiently different moveout characteristics as compared to the true phases. For example, the *S* and *sPPPP* phases for the 600-km-deep earthquake have nearly identical horizontal slowness (0.11s km^{-1}) at 65 degrees epicentral distance (Crotwell *et al*. 1999).

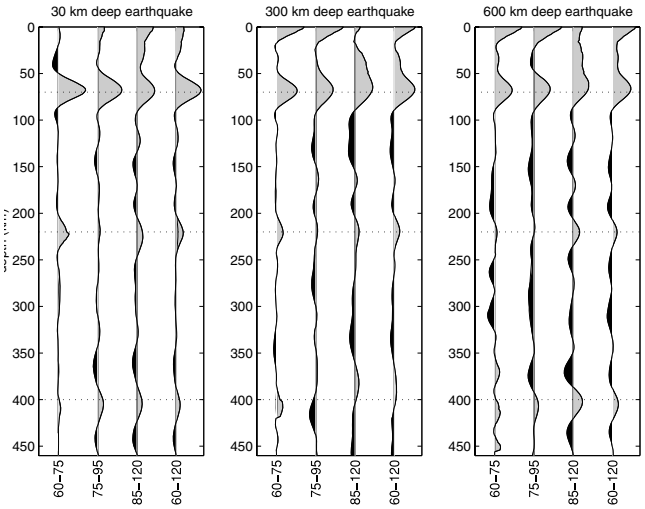

Figure8. Stacked traces from receiver functions shown in Figs5–7. Each stacked trace is labeled according to the epicentral distance range included in the stack.

Next we stack receiver functions computed from earthquakes with a range of epicentral distances and depths to test if this will provide additional noise cancellation. To provide an even greater range of earthquake depths for stacking we have computed additional synthetic data sets for earthquakes at 90, 180 and 450 km depth. Fig. 9 shows the results from stacking receiver functions from a range of epicentral distances and depths. Stacked receiver functions for the 60–75 degree epicentral distance range give the lowest noise levels of 2.9 per cent when only earthquakes less than 300 km depth are used, and 4.6 per cent when all depths are used (Table 1). Increasing the epicentral distance used in the stack increases the noise level for both depth stacking ranges, with noise levels up to 12.1 per cent for *SKS* arrivals for earthquakes shallower than 300 km and 11.5 per cent for *SKS* arrivals for earthquakes from all depths. Stacks using earthquakes from a range of depths generally have lower noise levels than stacks using only one depth with the exception of the 60–75 degree stacking range where the stack that includes all depths has a higher noise level (4.6 per cent) than the single depth stacks for the 30 and 300-km-deep earthquakes (3.9 and 2.8 per cent, respectively).

To test the ability of more sophisticated stacking techniques to achieve even lower noise levels, we employ bootstrap median stacking (e.g. Zoubir & Iskander 2004). For each set of receiver functions to be stacked we create 100 data subsets, with each subset containing a random resampling (with replacement) of the original receiver function data set. We then calculate the median receiver function for each subset, and finally we calculate the median of the subset medians to produce the final stacked receiver function. By randomly resampling the original receiver function data set, some of the re- sampled data subsets will be void of especially high noise receiver functions (outliers). Thus, when evaluating the median of this re- sampled data subset, we obtain a better estimate of the true median receiver function. The resulting bootstrap stacked receiver functions are shown in Fig. 10 and exhibit lower noise levels (Table 1) at all stacking distance ranges than the simple mean stacked traces shown in Fig. 9. The lowest noise levels (2.4 per cent) are achieved in the 60–75 degree stacking range using only earthquakes shallower than 300 km. In this same distance range when earthquakes from all depths are included the noise level increases to 3.7 per cent. It is important to recall that our synthetic data sets do not contain any actual background noise. The noise levels we are reporting here are from signal generated noise. Real data will also contain some level of background noise, which will

only be partially cancelled by stacking, thus resulting in higher noise levels. Also recall that our noise levels are relative to the Moho signal. This indicates that identification of seismic discontinuities that are only a few percent of the Moho discontinuity may not be possible with *Sp* receiver function methodology even in environments with very low background noise.

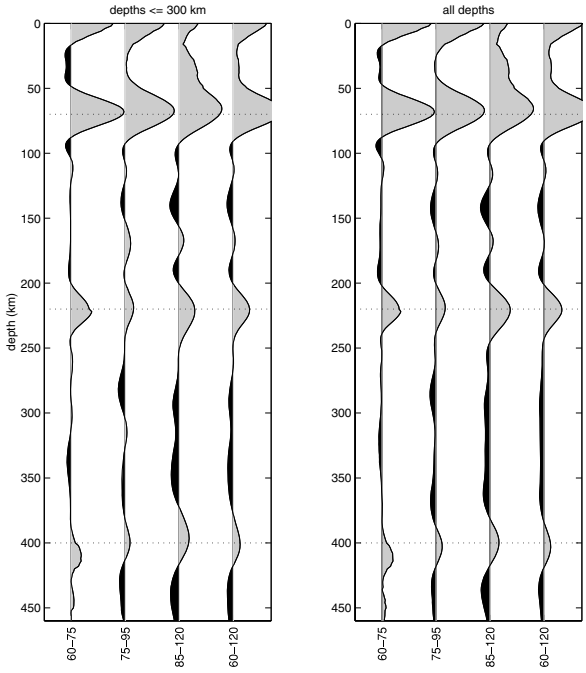

Figure 9. Stacked traces using receiver functions calculated from epicentres (a) shallower than 300 km depth and (b) from all depths. Each stacked trace is labelled according to the epicentral distance range included in the stack.

The successful cancellation of noise is dependent on the number of receiver functions included in the stack for both simple mean stacking and median bootstrap stacking. To quantify the dependence we have recalculated median bootstrap stacks for a range of receiver function data set sizes. The resulting noise levels as a function of receiver functions included in the stack are shown in Fig. 11. The lowest noise levels (2.4 per cent) are achieved for stacks using earthquake depths less than 300 km with the inclusion of approximately 20 receiver functions. However, when earth- quakes from all depths are used, low noise levels (3.7 per cent) are not achieved until approximately 40 receiver functions are included in the stack. A typical problem with temporary earthquake recording networks is that the deployment period is not sufficient to provide adequate data recording for analyses, which require a range of epicentral distances and/or azimuths (e.g. 3-D tomography resolution, amplitude variation with azimuth for analysis of anisotropy, etc.). This problem will be exaggerated in *Sp* receiver function processing if we restrict ourselves to earthquakes within the stacking range with the lowest noise (60–75 degrees epicentral distance; depth less than 300 km). For small *Sp* receiver function data sets it may be necessary to compute complete wavefield synthetics for each earthquake to aid in the identification of energy from sources other than the *S*-to-*P* converted phases of interest as suggested by Bock (1994).

To rule out the possibility that the observed multiply reflected phases in our synthetic seismograms are the result of insufficient levels of signal attenuation, and to verify the presence of multiply reflected phases in real data, we have created a stack of vertical component data from

deep (540–590 km) earthquakes recorded at all GSN and USNSN stations (Fig. 12). We observe several time windows of energy arriving from phases that have undergone multiple reflections off the Earth's surface, as well as energy arriving at the predicted time for the *PcPPcP* phase (two reflections off of the outer core). Phases with a first leg as an *S* wave (e.g. *sPPP*) are present as well as corresponding phases with a *P*-wave first leg (e.g. *pPPP*). However, in the synthetic data we primarily observed phases with a *P*-wave first leg. This discrepancy exists because the source orientation we have used for generating the synthetic seismograms was picked to optimize *S*v propagation at *S* and *SKS* take-off angles, and thus results in a source orientation that also efficiently propagates *P*-wave energy at *pPPP–pPPPPP* take-off angles. For the wide range of source mechanisms and orientations present in the real data, significant energy is to be expected for *sPPP– sPPPPP* phases. In a global study of *S*-to-*P* converted waves, Bock & Kind (1991) note that reliable identification of converted phases is significantly influenced by earthquake source orientation and mechanism. This suggests that *Sp* receiver function processing could be further improved by first identifying earthquakes that have strong *S*v radiation in the direction of the recording station.

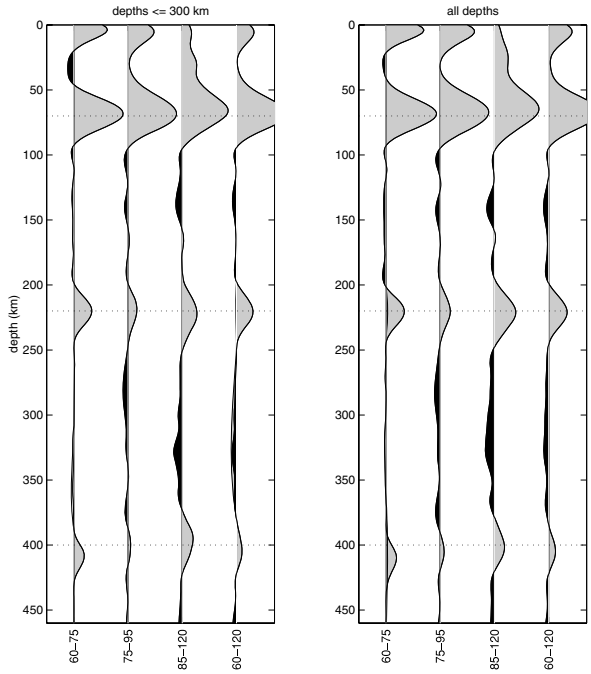

Figure 10. Stacked traces computed using median boot-strap stacking of receiver functions calculated from epicentres (a) shallower than 300 km depth and (b) from all depths. Each stacked trace is labelled according to the epicentral distance range included in the stack.

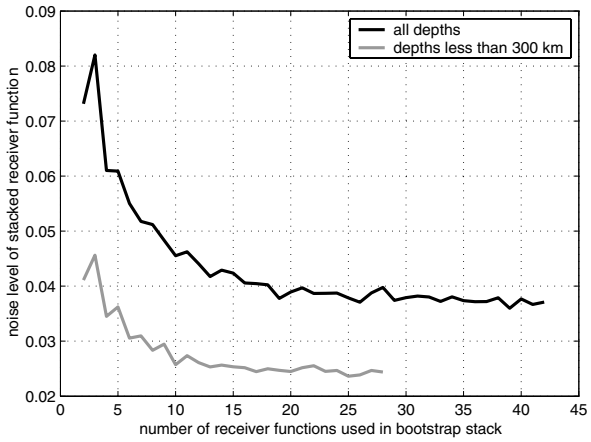

Figure 11. Noise levels for bootstrap stacked receiver function traces (from 60–75 degrees epicentral distance) as a function of number of receiver functions used in the stack.

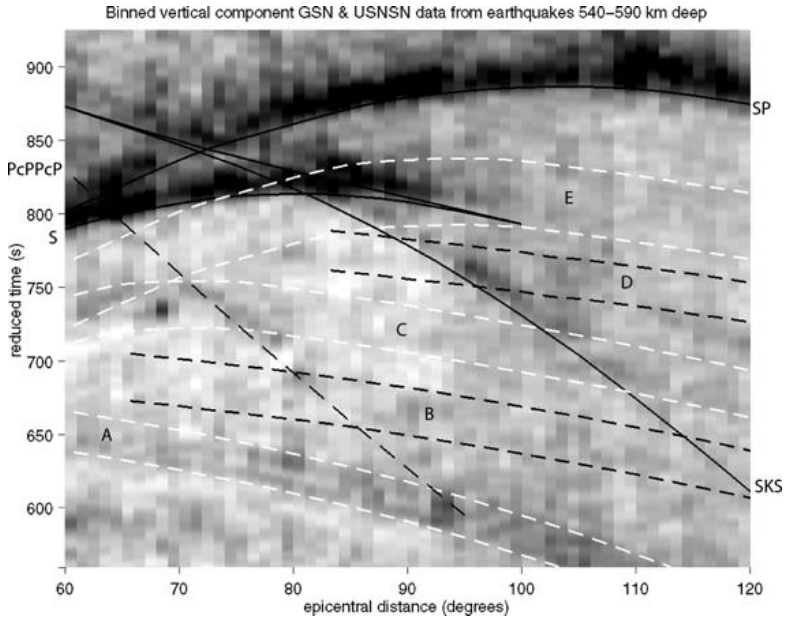

Figure 12. Stacked vertical component GSN and USNSN data for all earthquakes with depths between 540–590 km. Dashed lines indicate time windows for arrivals from (a) *sPP*, (b) *pPPP*, (c) *sPPP*, (d) *pPPPP* and (e) *sPPPP*.

5 CONCLUSIONS

A significant amount of interfering *P*-wave energy from multiply- reflected phases off the Earth's surface is observed immediately preceding the direct *S* arrival for deep focus earthquakes (600 km) resulting in *Sp* receiver functions with high noise levels. At epicentral distances of 75–95 degrees, there is significant overlap of *S* and *SKS* phases, which complicates source estimation in the receiver function deconvolution and may produce artefacts in the resulting receiver function. Furthermore, at this distance range, there is also an overlap of *Sp* and *SKSp* converted phase arrivals, which can pro- duce erroneous *Sp* receiver function phases. At epicentral distances

greater than 95 degrees for earthquakes at all depths, we find a significant level of interfering *P*-wave energy resulting from phases that have reflected multiple times off the Earth's surface. Receiver functions calculated from *SKS* arrivals at these distances exhibit a high level of erroneous receiver function phases. By stacking receiver functions that contain high levels of interfering *P*-wave energy it is possible to produce stacked images (e.g. a stack produced from primarily deep earthquakes) that contain considerable artifacts which may falsely appear as true earth structure (e.g. the lithosphere/asthenosphere boundary or low-velocity zones). To identify true receiver function phases in the presence of interfering *P*- wave energy, the phases must be observed over a range of earth- quake depths and epicentral distances. The lowest noise levels are achieved for *Sp* receiver function stacks using earthquake epicentral distances between 60–75 degrees and earthquake depths less than 300 km.

ACKNOWLEDGMENTS

Support for this work was provided by NSF grant EAR-0335782 and the John A. and Katherine G. Jackson School of Geosciences and the Geology Foundation at the University of Texas at Austin. Data shown in this study was obtained from the IRIS data management centre. The GSN and USNSN networks are maintained by Scripps Institution of Oceanography, Albuquerque Seismological Laboratory, and the USGS National Earthquake Information Center (NEIC).

REFERENCES

Ammon, C.J., 1991. The isolation of receiver effects from teleseismic *P*-wave-forms, *Bull. seism. Soc. Am.,* **81,** 2504–2510.

Baag, Chang-Eob & Langston, C.A., 1986. Diffracted Sp generated under the Australian Shield *J. geophys. Res.,* **91,** 9507–9576.

Bock, G., 1988. Sp phases from the Australian upper mantle, *Geophys. J.,* **94,** 73–81.

Bock, G., 1991. Long–period S to P converted waves and the onset of partial melting beneath Oahu, Hawaii, *Geophys. Res. Lett.,* **18,** 869– 872.

Bock, G., 1994. Multiples as Precursors to S, SKS, and ScS, *Geophys. J. Int.,* **119,** 421–427.

Bock, G. & Kind, R., 1991. A global study of S-to-P and P-to-S conversions from the upper mantle transition zone, *Geophys. J. Int.,* **107,** 117– 129.

Bostock, M.G. & Rondenay, S., 1999. Migration of scattered teleseismic body waves, *Geophys. J. Int.,* **137,** 732–746.

Clayton, R. & Wiggins, R., 1976. Source shape estimation and deconvolution of teleseismic body waves, *Geophys. J. R. Astr. Soc.,* **47,** 151– 177.

Crotwell, H.P., Owens, T.J. & Ritsema, J., 1999. The TauP toolkit; flexible seismic travel-time and ray-path utilities *Seis. Res. Lett.,* **70**(2), 154– 160.

Dziewonski, A.M. & Anderson, D.L., 1981. Preliminary reference Earth model, *Phys. Earth planet. Inter.,* **25,** 297–356.

Farra, V. & Vinnik, L., 2000. Upper mantle stratification by P and S receiver functions, *Geophys. J. Int.,* **141,** 699–712.

Farra, V., Vinnik, L.P., Romanowicz, B., Kosarev, G.L. & Kind, R., 1991. Inversion of teleseismic *S* particle motion for azimuthal anisotropy in the mantle: a feasibility study, *Geophys. J. Int.,* **106,** 421–431.

Fuchs, K. & Mueller, G., 1971. Computation of synthetic seismograms with the reflectivity method and comparison with observations, *Geophys. J. R. astr. Soc.,* **23,** 417–433.

Gutenberg, B., 1960. Waves reflected at the 'surface' of the earth–$P'P'P'P'$, *Bull. seism. Soc. Am.,* **50,** 71–79.

Husebye, E.S., Christofferson, A. & Frasier, C.W., 1975. Orthogonal representations of array–recorded short period *P*-waves, in *Exploitation of Seismograph Networks,* ed. Beauchamp, K.G., Nordhoff, Leiden.

Jordan, T.H. & Frazer, L.N., 1975. Crustal and upper mantle structure from SP Phases, *J. geophys. Res.,* **80,** 1504–1518.

Kind, R., 1985. The reflectivity method for different source and receiver structures, *J. Geophys.,* **58,** 146–152.

Kumar, P., Yuan, X., Kind, R. & Kosarev, G., 2005. The Lithosphere– Asthenosphere boundary in the Tien Shan–Karakoram region from S receiver functions—evidence of continental subduction, *Geophys. Res. Lett.,* **32,** L07305.

Langston, C.A., 1977. Corvallis, Oregon, crustal and upper mantle receiver structure from teleseismic *P* and *S* waves, *Bull. seism. Soc. Am.,* **67,** 713– 724.

Langston, C.A., 1979. Structure under Mount Rainier, Washington, inferred from observations of P to S converted waves, *J. geophys. Res.,* **84,** 4749– 4762.

Li, A., Fischer, K.M., van der Lee, S., Wysession, M.E., 2002. Crust and upper mantle discontinuity structure beneath eastern North America, *J. geophys. Res.,* **107,** doi:10.1029/2001JB000190.

Li, X., Kind, R., Priestley, K., Sobolev, S.V., Tilmann, F., Yuan, X. & Weber, M., 2000. Mapping the Hawaiian plume conduit with converted seismic waves, *Nature,* **405,** 938–941.

Li, X., Kind, R., Yuan, X., Wo ̈lbern, I. & Hanka, W., 2004. Rejuvenation of the lithosphere by the Hawaiian plume, *Nature,* **427,** 827–829.

Matsuzawa, T., Kono, T., Hasegawa, A. & Takagi, A., 1990. Subducting plate boundary beneath the northeastern Japan Arc estimated from SP converted waves, *Tectonophysics,* **181,** 123–133.

Oreshin, S., Vinnik, L. & Peregoudov, D., 2002. Lithosphere and asthenosphere of the Tien Shan imaged by S receiver functions, *Geophys. Res. Lett.,* **29**(8), 32-1–32-4.

Owens, T.J. & Zandt, G., 1997. Implications of crustal property variations for models of Tibetan plateau evolution, *Nature,* **387,** 37–43.

Owens, T.J., Zandt, G. & Taylor, S.R., 1984. Seismic Evidence for an Ancient Rift Beneath the Cumberland Plateau, Tennessee: A Detailed Analysis of Broadband Teleseismic P Waveforms, *J. geophys. Res.,* **89,** 7783–7795.

Sheehan A.F., Abers, G.A., Jones, C.H. & Lerner–Lam, A.L., 1995. Crustal thickness variations across the Colorado Rocky Mountains from teleseismic receiver functions, *J. geophys. Res.,* **100,** 20 391–20 404.

Vinnik, L.P., 1977. Detection of waves converted from P to SV in the mantle, *Phys. Earth planet. Inter.,* **15,** 39–45.

Vinnik, L.P. & Romanowicz, B.A., 1991. Origin of precursors to teleseismic S waves, *Bull. seism. Soc. Am.,* **81,** 1216–1230.

Vinnik, L., Kumar, M.R., Kind, R. & Farra, V., 2003. Super-deep low-velocity layer beneath the Arabian plate, *Geophys. Res. Lett.,* **30**(7), 1415.

Vinnik, L.P., Farra, V. & Kind, R., 2004. Deep structure of the Afro-Arabian hotspot by S receiver functions *Geophys. Res. Lett.,* **31,** L11608.

Vinnik, L.P., Foulger, G.R. & Du, Z., 2005. Seismic boundaries in the mantle beneath Iceland: a new constraint on temperature, *Geophys. J. Int.,* **160,** 533–538.

Wilson, D. & Aster, R., 2005. Seismic imaging of the crust and upper mantle using regularized joint receiver functions, frequency wave number filtering, and multimode Kirchhoff migration, *J. Geophys. Res.,* **110,** B05305, doi:10.1029/2004JB003430.

Wilson, D., Aster, R., Ni, J., Grand, S., West, M., Gao, W., Baldridge, W.S. & Semken, S., 2005. Imaging the seismic structure of the crust and upper mantle beneath the Great Plains, Rio Grande Rift, and Colorado Plateau using receiver functions, *J. geophys. Res.,* **110,** B05306, doi:10.1029/2004JB003492.

Wittlinger, G., Farra, V. & Vergne, J., 2004. Lithospheric and upper mantle stratifications beneath Tibet: new insights from Sp conversions, *Geophys. Res. Lett.,* **31,** L19615.

Yuan, X., Ni, J., Kind, R., Mechie, J. & Sandvol, E., 1997. Lithospheric and upper mantle structure of southern Tibet from a seismological passive source experiment, *J. geophys. Res.,* **102,** 27 491–27 500.

Zoubir, A.M. & Iskander, D.R., 2004. Bootstrap Techniques for Signal Processing, *Cambridge University Press,* Cambridge, UK, ISBN-0-521- 83127-X.